Pulsating Tandem Microbubble for Localized and Directional Single-Cell Membrane Poration

G. N. Sankin, F. Yuan, and P. Zhong*

Department of Mechanical Engineering and Materials Science, Duke University, Box 90300, Durham, North Carolina 27708, USA
(Received 17 May 2010; revised manuscript received 28 June 2010; published 9 August 2010)

The interaction of laser-generated tandem microbubble (maximum diameter of about 50 μm) with single (rat mammary carcinoma) cells is investigated in a 25-μm liquid layer. Antiphase and coupled oscillation of the tandem microbubble leads to the formation of alternating, directional microjets (with max microstreaming velocity of 10 m/s) and vortices (max vorticity of $350\,000$ s^{-1}) in opposite directions. Localized and directional membrane poration (200 nm to 2 μm in pore size) can be produced by the tandem microbubble in an orientation and proximity-dependent manner, which is absent from a single oscillating microbubble of comparable size and at the same stand-off distance.

Introduction.—Cavitation, the formation and dynamics of vapor or gas bubbles in aqueous medium, plays a pivotal role in a diverse range of biomedical and engineering applications [1,2]. An oscillating bubble can release energy upon symmetric collapse in the form of heat, light, and shock wave, [3] or a high-speed liquid jet due to bubble-bubble interaction [4], asymmetric collapse either near a boundary [2] or under the influence of an impinging shock wave [5]. In contrast to damaging ship propellers and hydraulic structures [6], the power of cavitation has often been harnessed in biomedical applications for the treatment of cancers by high-intensity focused ultrasound, non-invasive disintegration of kidney stones by shock wave lithotripsy, and ultrasound-mediated drug and gene delivery [1]. However, understanding the dynamic bubble-cell interaction and its causal relation with the biological consequences still remains to be a significant challenge. Only a few studies have been performed to investigate bubble-cell interaction under well-controlled experimental conditions, using either a small air bubble [7,8] or ultrasound contrast agents as stabilized cavitation nuclei [9] in an acoustic field, or a laser-generated millimeter- and micron-size bubble to interact with adherent [10] or suspension [11] cells. Overall, these previous studies are limited in resolving the transient bubble-cell interaction, associated fluid dynamics, and membrane poration by the cavitating bubble, as well as subsequent transport of macromolecule into the cell.

In this Letter, we introduce a method for generating tandem microbubble in close proximity that leads to alternating formation of microjets in opposite directions. The transient bubble-bubble and microjet-cell interaction, as well as resultant microstreaming and vortex formation are characterized by high-speed imaging and microparticle image velocimetry (μPIV). Using this method, localized and directional membrane poration in single biological cells can be produced in an orientation and proximity-dependent manner.

Experimental setup.—A Zeiss Axio Observer inverted microscope was configured to incorporate two laser beams for tandem microbubble generation and high-speed cameras for imaging of bubble dynamics, bubble-cell interaction, and μPIV of fluid motion [Fig. 1(a)]. Two Q-switched Nd:YAG lasers of 5 ns pulse duration [MiniLase I (LASER1) and Solo PIV (LASER2), New Wave Research] with wavelength of 1064 nm and 532 nm, respectively, were transmitted through a 63$\times$ long-working-distance objective. The incident angle of LASER1 was slightly tilted so that the foci of the two laser beams were separated by a distance of $\Delta = 40$ μm. Each laser beam (~ 30 μJ) is preferentially absorbed by the fluid medium containing 0.4% Trypan blue in a microfluidic channel [Fig. 1(b)], generating a microbubble via optical breakdown [11]. By controlling the release of individual laser pulses using a digital delay generator (BNC 555, Berkeley Nucleonics Corporation), tandem microbubbles with different oscillation phases can be produced.

High-speed imaging and μPIV.—Two 45°-dichroic mirrors (900dcsp and z532dcrb, Chroma) were used for reflection of the laser beams and simultaneous transmission of illumination light for high-speed imaging. A fiber-optic coupled Xenon flash lamp (ML1000, Dyna-Lite) was used to provide backlight illumination, petitioned into an 80/20 intensity ratio between two high-speed cameras (Imacon 200, DRS Hadland and Phantom v7.3, Vision Research). The Imacon 200 was operated at 1×10^6 frames per second, 50 ns exposure time, and 14 frames per sequence to capture the dynamics of bubble-bubble-cell interaction. The Phantom camera was used to record the subsequent uptake and progressive diffusion of Trypan blue into the targeted cell within 1 min. Moreover, a Shimadzu HPV-1 camera operated at 1×10^6 frames per second, 250 ns exposure time, and 100 frames per sequence was used for μPIV. For flow visualization, 2 μm polystyrene beads (R0200, Duke Scientific) were added in the medium as tracers at 1×10^9 beads/ml concentration. The acquired images were processed using DaVis 7 software (LaVision, GmbH) for determining the velocity field around pulsating microbubble(s).
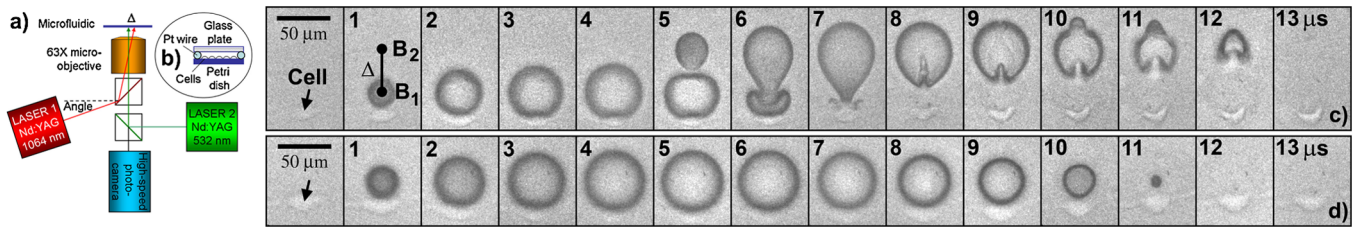
FIG. 1 (color online).   Dynamics of tandem microbubble and bubble-cell interaction. (a) Experimental setup. Microbubbles are generated by two pulsed Nd:YAG lasers, which are separated by $\Delta = 40$ μm in the focal plane of a $63\times$ objective. (b) Microfluidic exposure chamber with 25 μm in height, 10 mm $\times$ 25 mm in channel width and length. (c) Dynamics of tandem microbubble (generated by both lasers with a 4 μs interpulse delay) and their interaction with an adherent cell (pointed to by arrow) near the first bubble (B_1). (d) Dynamics of single microbubble (generated by LASER1) and its interaction with an adherent cell (pointed to by arrow). The asymmetric deformation with resultant formation of alternating microjets in opposite directions along the tandem microbubble axis (movie 1 in the supplementary material [15]) is not observed during the symmetric expansion and collapse of the laser-generated single microbubble of comparable size (movie 2 in the supplementary material [15]).

Cell culture and experimental design.—Rat mammary carcinoma cells maintained routinely in culture (37 °C) were trypsinized and reseeded in a 60-mm diameter Petri dish at 10^5 cells/ml concentration one day before the experiment. When cell growth reached about 10% confluence, the culture medium was replaced by saline solution containing 0.4% Trypan blue (T8154, Sigma-Aldrich) at room temperature (~ 20 °C). Subsequently, two 25-μm platinum wires (A-M Systems) were placed in parallel in the Petri dish to form a channel of $\sim$10 mm wide and 25 mm long. A 1.0-mm thick glass plate was then placed on top of the platinum wires to form a microfluidic exposure chamber [Fig. 1(b)]. Trypan blue enhanced laser absorption to facilitate optical breakdown while providing concomitantly a biomarker for membrane poration.

Adherent cells of spindle shape were selected and randomly assigned to one of the seven groups. Cells in groups G_1 to G_3 were treated at different orientations (0° and 90°) with respect to tandem microbubble axis while maintaining the same stand-off distance (SD) of 10 μm. Cells in groups G_4 to G_6 were treated at SD = 20, 30, and 40 μm, respectively, while maintaining the same orientation (0°, as used in case G_1). In group G_0 (control), cells were treated by a single bubble (B_1) produced at SD = 10 μm.

Bubble-bubble and microjet-cell interaction.—Similar to shockwave-bubble interaction [12,13], the most effective energy transfer is produced when the collapse time of the bubble matches with the duration of external driving force. By releasing the two laser pulses in tandem with a 4 μs interpulse delay, a first bubble (B_1) can be generated (at time = 0 μs) that expands to a maximum size of about 50 μm before a second bubble (B_2) of similar size is produced [Fig. 1(c), 4 μs]. Consequently, the collapse of B_1 is coupled with the simultaneous expansion of B_2, leading to asymmetric deformation of the bubbles with microjets formation [Fig. 1(c), 6 μs] under the influence of secondary Bjerknes forces [14]. Thereafter, B_2 begins to collapse with its elongated portion in contact with B_1 contracting rapidly, producing a second microjet moving away from B_1 [Fig. 1(c), 8 $\sim$ 12 μs]. This alternating

formation of microjets moving in opposite directions along the axis of the tandem microbubble (movie 1 in the supplementary material [15]) is not observed during the symmetric expansion and collapse of a single microbubble (movie 2 in the supplementary material [15]) of comparable size produced by one laser [Fig. 1(d)]. Similar bubble dynamics have been observed in an unconstrained fluid medium using spark-generated vapor bubbles of millimeter size [16].

Flow field around the pulsating microbubble(s).—Following the 1st optical breakdown, the fluid is initially pushed outward from the center of B_1 before reversing the direction of flow during subsequent collapse after the maximum bubble expansion (movie 3 in the supplementary material [15]). In contrast, the initial symmetric expansion of B_2 is quickly distorted with its proximal end being sucked in by the collapsing B_1, leading to the formation of the first microjet [J_1 in Fig. 2(a), 6 μs]. The acceleration of J_1 produces a microstreaming impulse with a maximum flow velocity on the order of 10 m/s near the jet tip (5 to 6 μs). Upon maximum expansion, the elongated B_2 collapses asymmetrically and generates the second microjet (J_2) that moves away from B_1 (7 to 11 μs). As a consequence of the alternating microjet formation, two pairs of vortices are generated around B_1 and B_2, one rotating clockwise and the other counterclockwise [Fig. 2(b)], reaching a maximum vorticity of 350 000 s^{-1} at 6 μs. Vortex formation from laser-induced single bubble ($\sim$150 μm in diameter) near a microfludic channel wall was recently reported with a maximum vorticity of 100 000 s^{-1} [17].

Cell membrane poration.—Because of the unique flow pattern produced by the pulsating tandem microbubble, we examined its influence on the morphology and membrane permeability of individual adherent cells (Rat mammary carcinoma) placed nearby. As shown in Fig. 3(a), a cell placed on the axis of B_1 and B_2 with a SD of 10 μm from the proximal surface of B_2 (case G_2) can be deformed significantly [see Fig. 2(a) for an example of case G_1] while its counterpart in the symmetric flow field of a single
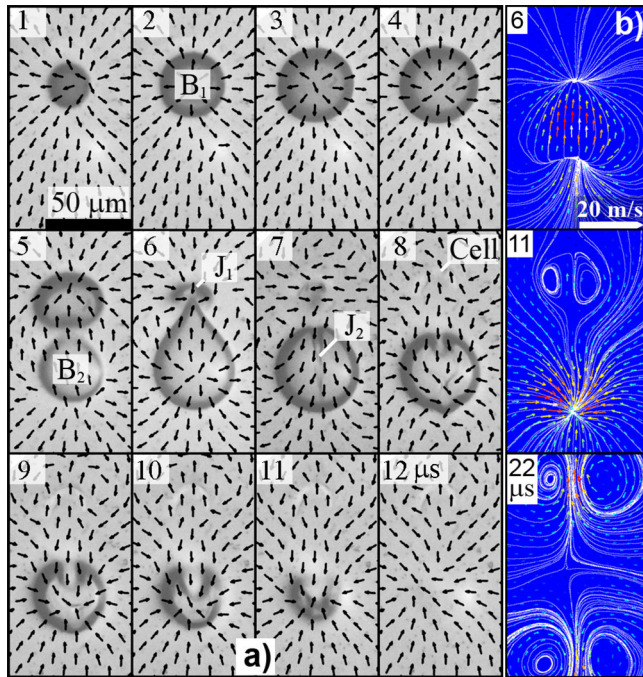
FIG. 2 (color online).   Fluid motion. (a) High-speed imaging of bubble dynamics and micro-particle image velocimetry (μPIV) using 10×10 μm interrogation windows with 25% overlap indicating the flow direction around individual oscillating microbubbles. Flow tracers (i.e., 2 μm polystyrene beads) were used to facilitate visualization of the velocity field. (b) Streamline display of three μPIV images, demonstrating vortex formation in the flow field, with one pair of vortices rotating clockwise and the other counterclockwise within 22 μs (movie 3 in the supplementary material [15]) following the generation of the tandem microbubble.
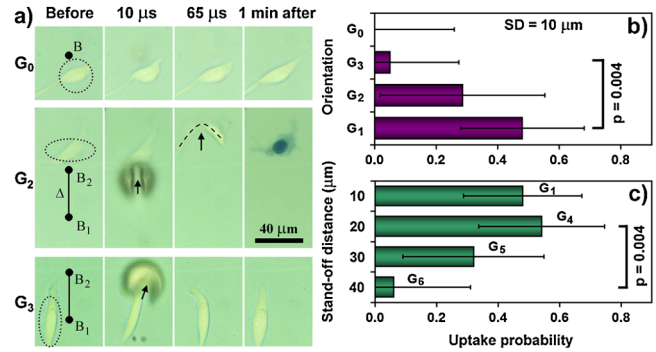

FIG. 3 (color online).   Trypan blue uptake. (a) Cell deformation produced by the microjet and vortex flow initiated from the pulsating tandem microbubble. Representative images of individual cells (circled) before, at 10 and 65 μs, and 1 min after the interaction with either single (case G_0) or tandem (case G_2 or G_3) microbubble. (b) Probability of Trypan blue uptake in 1 min after microbubble-cell interaction: effect of orientation (G_1, impacted by J_1; G_2, impacted by J_2; and G_3, parallel to J_1). The stand-off distance between the proximal cell surface and bubble center is 10 μm. (c) Probability of Trypan blue uptake in 1 min after microbubble-cell interaction: effect of stand-off distance. Individual cells are located on the axis of the tandem microbubble, with a bubble-cell stand-off distance varying from 10 μm to 40 μm, at an interbubble separation distance $\Delta = 40$ μm. Error bars indicate intervals $\pm 1/\sqrt{N}$, where N (=15 to 27) is the number of cells treated in each group. Two-tailed test of proportions was used for statistical analysis for comparing results between different groups.

bubble is only strained mildly (case G_0). The microjet-flow-cell interaction along the tandem bubble axis causes a micron-scale bending and shear deformation of the cell [65 μs in Fig. 3(a) for case G_2] that leads to localized membrane disruption and uptake of Trypan blue within 1 min. In comparison, when a cell is placed at the same SD but rotated by 90° from the axis of B_1 and B_2 [Fig. 3(a), case G_3] or subjected to the symmetric expansion and collapse of a single bubble (case G_0), a much milder strain with no concomitant Trypan blue uptake is observed. Also, no appreciable membrane poration is produced when the cell is located either off the tandem microbubble axis with a SD greater than 10 μm or on the axis with a SD greater than 40 μm. Quantitatively, the membrane poration produced by the tandem microbubble shows a clear dependence on orientation [Fig. 3(b)] and stand-off distance [Fig. 3(c)]. Statistically significant ($p < 0.05$) increase in Trypan blue uptake is observed in G_1 and G_4 compared to G_3 and G_6, respectively, with maximum probability for Trypan blue uptake produced at SD = 20 μm along the tandem microbubble axis.

Localized and directional membrane poration.—The membrane disruption is highly localized. Using time-lapse

imaging [Fig. 4(a)], we can observe a pinpoint entrance of the Trypan blue from the cell surface proximal to the jet impact in 6 s. The dye gradually diffuses and spreads out in the cytosol towards the distal end in 24 s, with subsequent directional entrance and staining of the cell nuclei by 42 s (movie 4 in the supplementary material [15]). Using our setup, the cell can be quickly fixed by a perfusion flow of 2.5% glutaraldehyde, started in about 10 seconds after the tandem microbubble-cell interaction. Subsequently, cell location and jet impact direction are registered by laser-produced markings at the bottom of the Petri dish [Fig. 4(b)]. Scanning electron microscopy of the treated cell reveals highly localized membrane disruption with single or dual pore formation at the site of membrane surface facing the microjet impact. The pore size varies from 200 nm to 2 μm [Figs. 4(c) and 4(d)]. Because the cell is treated in Trypan blue solution (with no Ca^{2+} content), active repair of the pore is likely to be significantly compromised with smaller than 1 μm spherical vesicles observed at the disruption site [see Fig. 4(d)] [18,19]. Therefore, the observed pore size may represent an upper limit in membrane disruption produced by the tandem microbubble under physiological conditions.

Discussion and summary.—A new method is developed to produce localized and directional membrane poration on single cells with high precision and reproducibility. The pore size can be varied from nanometer to micrometer
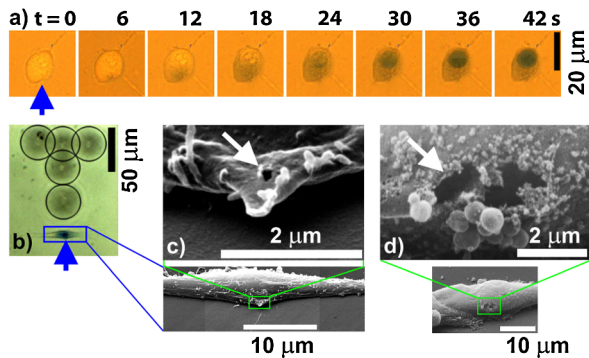
FIG. 4 (color online). Membrane poration. (a) Time-elapse images showing pinpoint entrance of Trypan blue into the cell from the site of microjet impact (pointed to by arrow) with subsequent progressive diffusion in the cytosol and staining of the nuclei (movie 4 in the supplementary material [15]). (b) Laser-generated marking dots (circled) on the bottom surface (~1.0 mm thick polystyrene) of the Petri dish, which are used to register the treated cell, site and direction (distal to "T" marking) of the microjet impact. (c) SEM images of the porated cell shown in (b), demonstrating the formation of a 200 nm pore (pointed by arrow) at the site of microjet impact. (d) SEM images of another porated cell, showing the formation of two adjacent pores (pointed to by arrow) of about $1 \sim 2 \ \mu m$ in individual pore size. Spherical vesicles of less than 1 μm in size were observed near the disruption site, which is characteristic of cell membrane resealing after mechanical damage without Ca^{2+} in the surrounding medium.

range, limited only by the ability of the cell to reseal the disruption site [19]. Because jet diameter is usually about one-tenth of the maximum bubble size, the potential energy accumulated by a single bubble with comparable size to a cell (i.e., ~20 μm) is limited and insufficient to produce measurable membrane disruption when collapsing near a boundary [20]. By confining the bubble generation in a quasi-2D thin layer, and furthermore, by transferring and focusing energy through tandem microbubble interaction, we have demonstrated the feasibility for generating pinpoint mechanical forces for highly localized membrane poration.

Microjetting induced flow shear stress and resultant bending (and stretching) of the cell body may contribute to the observed pore formation. The flow-induced shear stress (τ) near the microfluidic channel (height = $2h = 25 \ \mu m$) surface can be estimated by $\tau = \mu(V_j/h)$ where μ is dynamic viscosity of the medium and V_j is jet speed. The estimated maximum shear stress in our setup is about 1 kPa, which is within the range of previously reported critical shear stress of 0.1 kPa for cell detachment [20] and water-hammer pressure of 3 kPa for jet impact induced membrane rupture [9].

Individual cells placed on the axis of the tandem microbubble [see Figs. 1(c), 2(a), and 3(a)] show different de-grees of bending deformation produced by jet impact and resultant microstreaming and vortex flow. The central portion of the cell directly under jet impact is detached, while one or both distal ends of the cell remain attached, leading to a significant stretching of the cell membrane. The stretching ratios of material lines located at different orientations and SDs from the tandem microbubble (data not shown), estimated based on μPIV images, show a good correlation with the membrane poration.

It is envisioned that the technique developed in this work can be easily integrated in microfluidics and thus possessing great potential in high-throughput biosynthesis and bioengineering applications, and for mechanistic investigation of cavitation-induced bioeffects.

*Corresponding author: pzhong@duke.edu
[1] S. Mitragotri, Nat. Rev. Drug Discov. **4**, 255 (2005).
[2] J. R. Blake and D. C. Gibson, Annu. Rev. Fluid Mech. **19**, 99 (1987).
[3] C. D. Ohl *et al.*, Phil. Trans. R. Soc. A **357**, 269 (1999).
[4] P. A. Quinto-Su *et al.*, Phys. Rev. Lett. **104**, 014501 (2010).
[5] J. P. Dear, J. E. Field, and A. J. Walton, Nature (London) **332**, 505 (1988).
[6] R. E. A. Arndt, Annu. Rev. Fluid Mech. **13**, 273 (1981).
[7] J. A. Rooney, Science **169**, 869 (1970).
[8] P. Marmottant and S. Hilgenfeldt, Nature (London) **423**, 153 (2003).
[9] P. Prentice *et al.*, Nature Phys. **1**, 107 (2005).
[10] R. Dijkink *et al.*, Phys. Med. Biol. **53**, 375 (2008).
[11] S. Le Gac *et al.*, Lab Chip **7**, 1666 (2007).
[12] G. N. Sankin *et al.*, Phys. Rev. Lett. **95**, 034501 (2005).
[13] G. N. Sankin and P. Zhong, Phys. Rev. E **74**, 046304 (2006).
[14] G. L. Chahine and R. Duraiswami, J. Fluids Eng. **114**, 680 (1992).
[15] See supplementary material at http://link.aps.org/supplemental/10.1103/PhysRevLett.105.078101 for movies.
[16] B. C. Khoo *et al.*, Mod. Phys. Lett. B **23**, 229 (2009).
[17] E. Zwaan *et al.*, Phys. Rev. Lett. **98**, 254501 (2007).
[18] Y. Zhou *et al.*, J. Control. Release **126**, 34 (2008).
[19] P. L. McNeil and R. A. Steinhardt, Annu. Rev. Cell Dev. Biol. **19**, 697 (2003).
[20] C. D. Ohl and B. Wolfrum, Biochim. Biophys. Acta **1624**, 131 (2003).